Vortex Domain Walls in Ferroelectrics

Z. Hong[1,2*], S. Das[3*], C. T. Nelson[4*], A. Yadav[3], Y. Wu[1], J. Junquera[5], L.-Q. Chen[2], L. W. Martin[3,6], R. Ramesh[3,6,7]

[1] Laboratory of Dielectric Materials, State Key Laboratory of Silicon Materials, Cyrus Tang Center for Sensor Materials and Applications, School of Materials Science and Engineering, Zhejiang University, Hangzhou, Zhejiang 310027, China

[2] Department of Materials Science and Engineering, The Pennsylvania State University, University Park, Pennsylvania 16802, USA

[3] Department of Materials Science and Engineering, University of California, Berkeley, California 94720, USA.

[4] Oak Ridge National Laboratory, Bethel Valley Rd., Tennessee 37831-6071, USA

[5] Departamento de Ciencias de la Tierra y Física de la Materia Condensada, Universidad de Cantabria, Cantabria Campus Internacional, Avenidad de los Castros s/n, E-39005 Santander, Spain

[6] Materials Sciences Division, Lawrence Berkeley National Laboratory, Berkeley, California 94720, USA.

[7] Department of Physics, University of California, Berkeley, California 94720, USA.

(* authors contributed equally)

Controlling domain formation in ferroelectric materials at the nanoscale is a fertile ground to explore emergent phenomena and their technological prospects. For example, charged ferroelectric domain walls in $BiFeO_3$ and $ErMnO_3$ exhibit significantly enhanced conductivity which could serve as the foundation for next-generation circuits[1]. Here, we describe a concept in which polar vortices perform the same role as a ferroelectric domain wall in classical domain structures with the key difference being that the polar vortices can accommodate charged (*i.e.*, head-to-head and tail-to-tail) domains, for example, in ferroelectric $PbTiO_3$/dielectric $SrTiO_3$ superlattices. Such a vortex structure can be manipulated in a reversible fashion under an applied field, manifesting as large changes in the local dielectric permittivity.

Interfaces offer vast permutations on material properties and coupling effects. One example is the formation of domain walls in ferroic materials, *i.e.*, the transition regions that separate differently oriented regions of ferroic order –magnetic moment (***M***) in ferromagnets, strain (***ε***) in ferroelastics, and electric polarization (***P***) in ferroelectrics. The chemical homogeneity of domain walls combines their local functionality with a spatial location which is readily manipulated via external fields. For instance, imparting "charged" configurations such as head-to-head domain junctions in confined ferromagnetic strips can produce complex topologies such as vortex domain walls (VDWs)[1] which can serve as functional elements in solid-state magnetic memories[2] or spin-logic[3,4] devices. The formation of complex-spin topologies in magnetic layers is driven by the competition between symmetric and antisymmetric exchange interactions (*e.g.*, Dzyalozhinski-Moriya interactions, DMI). In proper ferroelectrics such as $PbTiO_3$, however, the large ***P*** is a result of the non-centrosymmetric ionic positions that produce a net dipole moment.[5] In the absence of an equivalent mechanism to that of the DMI in magnets, it is typically thought that proper ferroelectrics form narrow-width, Ising-like domain walls as a consequence of the large crystalline anisotropy and the ability to scale polarization through a $\boldsymbol{P} = 0$ paraelectric structure[6]. It has been discovered recently, however, that ferroelectric domain walls can exhibit rotational components[7] including a pronounced Néel character in the vicinity of the domain wall where minimization of stray-field energies leads to wall broadening[8] and the formation of rotational flux-closure structures[9, 10] including closed loops.[11]

The three prototypical walls (Fig. S1A) are classified by either their axis of rigid rotation (Néel vs. Bloch type) or the scaling of the order parameter through the wall (Ising type). A primary approach to functionalize domain walls is by imposing a divergence of the ferroic-order parameter ($\nabla \cdot F \neq 0$), *i.e.*, either a "source" (tail-to-tail) or "drain" (head-to-head) of flux. The maximum/minimum divergence corresponds to a 180° head-to-head or tail-to-tail domain wall normal to the polarization axis and is promoted through sample geometries such as axially polar nanowires/nanostrips poled with endpoint domains in 180° opposition (Fig. S1B). For magnetic systems, which are inherently constrained by the well-known Maxwell equations, *e.g.*, $\nabla \cdot B = 0$, multiwall structures including VDWs, multi-VDWs, and/or transverse-domain walls are possible depending on the material properties and their length scale.[12] For polar materials, unsurprisingly, the formation of domain-wall types depends largely on the screening mechanisms of the insulating ferroelectric host phase as well as the mechanical boundary conditions.[13, 14] Such ferroelectric domain walls can exhibit significantly modified local conductivity,[15-18] and predominantly manifests in materials with smaller polarization (*i.e.*, lower divergence of $\boldsymbol{P}$ at the wall). Recently, it has been discovered that screening mechanisms can stabilize "charged" domain walls (CDWs) which themselves exhibit anomalous conductivity[1,15-21] and novel electronic phases.[18] A polar vortex, the analog of a magnetic vortex, appears in a much smaller size as observed recently in ferroelectric heterostructures[22-24]. However, to the best of our knowledge, VDWs built from electrical polarization, have not been reported and would represent a new class of topologically complex domain walls with potential advantages in direct electric-field manipulation of features with intrinsically smaller length scales than their magnetic counterparts. Moreover, creating and erasing VDWs provides a mechanism for deterministic local control of toroidal-ferroelectric order and accompanying phenomena such as conductivity[25], toroidal order[26], negative capacitance[27] and chirality.[28]

Herein, we employ the ferroelectric/dielectric superlattice (*i.e.*, $(PbTiO_3)_m/(SrTiO_3)_m$ m = 6-16 unit cells) as a model system to study the formations of VDWs in ferroelectrics. The superlattices are grown on $DyScO_3$ $(110)_O$ substrates with a 5-nm-thick $SrRuO_3$ buffer electrode by reflection high-energy electron diffraction (RHEED)-assisted pulsed-laser deposition (Methods). We observe that VDWs are formed to accommodate large electrostatic gradients created by tail-to-tail and head-to-head wall configurations of the ferroelectric domains on either side. For instance, $(PbTiO_3)_6/(SrTiO_3)_6$ superlattices have a stable rigid toroidal topology[28] consisting of a mixed-phase state of an ordered array of alternate clockwise-anticlockwise vortices and classical ferroelectric a_1/a_2 domains in the $PbTiO_3$ layers (Fig. 1A). Cross-sectional, dark-field transmission electron microscopy (TEM) images show the coexistence of vortex arrays (bright/dark modulation corresponding to the period of the repeating clockwise-anticlockwise vortices) and the in-plane polarized *a*-domains (Fig. 1B). This is the result of the competition between the elastic, electrostatic, and domain-wall energies that together favor a polydomain mix of in-plane and out-of-plane polarization within the interacting vortex arrangements. As in the macroscale, the phase separates into roughly periodic blocks of vortices and *a* domains such that the VDWs form on $\{101\}_{pc}$.

To explore the feasibility of CDWs as progenitors of VDWs, phase-field simulations have been performed on a $(PbTiO_3)_6/(SrTiO_3)_6$ superlattice by solving the time-dependent Ginzburg-Landau equation (Methods). The pre-designed CDW relaxes into a mixed polarization structure similar to the experimental geometry, consisting of *a* domains, wavy spirals, and inclined vortex domains. Head-to-head, tail-to-tail, and, in some rare cases, neutral boundaries between in-plane-oriented *a* domains are found to be stabilized with bridging vortex structures. The *a* domains and the vortex arrays have a well-defined boundary along the $[101]_{pc}$, which is reminiscent of a 90° *a*/*c*-type twin domain wall. The formation of a vortex state between the head-to-head (tail-to-tail) portions of the layers is largely due to the need to accommodate the large electrostatic energy associated with a charged interface, while the formation of the vortex state between the neutral (*e.g.*, head-to-tail) portions of the layers is due to the elastic energy as well as the polarization permutation between the neighboring layers in the ultrashort-period structure. The evolution pathway of the VDW calculated by phase-field simulations is elaborated upon in the supplementary materials (Fig. S2), which shows the formation of an intermediate metastable state with only one and two vortices in between the head-to-head (tail-to-tail) portions of the layers. This indicates the possibility to further reduce the number of transitional vortices through control of the elastic energy (via tuning of film thickness, substrate, thermal mismatch, etc.), as well as to control the number of vortices through external mechanical, thermal, or electrical forces.

To get a magnified view of the VDW boundary, we focus on a single $PbTiO_3$ layer. The polar displacement vectors ($\boldsymbol{P}_D$, indicated by arrows, Fig. 2A, B) overlaid on the cross-sectional high resolution-scanning TEM (STEM) image indicates a mixed structure with alternating clockwise and anticlockwise vortices and *a* domains. Notably, the presence of vortices in the $PbTiO_3$ layers is laterally bound by antiparallel *a* domains that would nominally form a charged domain wall (head-to-head or tail-to-tail), which would give rise to a large electrostatic energy (Fig. 2A, B). The formation of vortices is an elegant way to accommodate this electrostatic energy. The connection between the vortices and *a*-domain structures is made via the vertical offset of a boundary half-vortex. The corresponding high-resolution image from the phase-field simulation (Fig. 2C) shows the formation of VDW's to accommodate both head-to-head and tail-to-tail domains. A half-vortex structure acts as the connection between the vortices and *a* domains, similar to the experimental observations. Notably, due to the electrostatic interaction, the *c*-like regions in the vortices of the two neighboring layers can penetrate through the intermediate $SrTiO_3$ layer, giving rise to ordering of the vortices in the adjacent layers, which is also indicated in experimental observations (Fig. 1B. It is interesting to note that the number of bridging vortices does not need to be an even number, *i.e.*, they are not required to form pairs in this configuration, which could give rise to a net toroidal moment in one $PbTiO_3$ layer.

In order to show the feasibility of controlling the formation and deletion of the VDWs, we explored the phase evolution in TEM under an electric bias applied through a tungsten tip to the grounded bottom electrode, across a $(PbTiO_3)_6/(SrTiO_3)_6$ superlattice (Fig. 3; details in Methods). The field distribution under this tip (Fig. S3) was simulated using a Lorentz-type distribution,[29] with a tip radius of ~20 nm. Experimentally, after applying +15 V, the majority of the VDWs are eliminated, forming in-plane polarized *a*-like domains under the tip which are directed antiparallel to the charge of the tip (Fig. 3A). When the field is removed, the VDWs are recovered. Under an applied bias of -15 V, in-plane polarized CDWs are again formed with the polarization directions now pointing towards the tip. Removal of the negative bias, again, leads to the recovery of the vortex state. The in-plane electric field (defined by the negative of the gradient of the surface electric potential, *i.e.*, $E=-\nabla\varphi$) is pointing towards the tip while it is pointing away from the tip when it is positive (Fig. S3). The same evolution is observed in the phase-field simulations (Fig. 3B, magnified view given in Fig. 3C) and in experiments (Fig. 3A), which confirms the reversible switching between the in-plane polarized CDW and the VDW state with externally applied electric field, showing the possibility of the controllable switching between these two states.

These results shed light on an interesting conceptual possibility in which an external electric field can reversibly switch between the vortex-domain state and a uniformly polarized state, analogous to a conventional domain wall separating regions of opposite polarization. The dielectric response of such a rudimentary device (Fig. 4) shows a large change in the out-of-plane permittivity, (by 50%), as a consequence of the field-driven changes from the vortex structure to the uniformly poled domain, as evidenced by both phase-field simulations (Fig. 4A) and experimental observations (Fig. 4B).

In summary, we have demonstrated the formation of VDWs in ferroelectric superlattices of $PbTiO_3/SrTiO_3$ with both experimental observations with (S)TEM and theoretical calculation by phase-field simulations. This VDWs acts like a “bridge” for CDWs, with controllable local transitions between the VDWs and the CDWs that result in large tunability in dielectric properties. This solves a key complication in manipulating these structures, where simple static electric-field distribution cannot promote such formation. Instead, a static electric field distribution induces a high-energy configuration which spontaneously adopts an energetically accessible toroidal configuration, as occurs for ferromagnets in similar stripe geometries.[30] The relative vortex stability also depends on the different length scales of the layers, propagating into large domains or forming discrete vortex strings, respectively. Realization of discrete vortex strings structures represents an important step in these ferroelectric complex topologies, analogues to the ferromagnetic vortex domain walls. The former provides a mechanism for the experimentally observed writing of vortex domains under a biased PFM tip in bulk films.[26]

Regardless, this system now provides a platform where these dynamics and properties can be explored. Further reduction of the vortex numbers and separating single vortex state can be further explored by manipulating the film thickness and substrate lattice constant, etc. We hope that this study will spur more interest in VDW memory systems.

Materials and Methods

Superlattices Growth. The $(PbTiO_3)_n/(SrTiO_3)_n$ (n =6, 8, 16 monolayers) superlattices of were synthesized on 5 nm $SrRuO_3$-buffered, single-crystalline $DyScO_3$ (011) substrates via RHEED assisted pulsed-laser deposition. The growth temperature and oxygen pressure of the $SrRuO_3$ layer was accomplished at 750°C and 50 mTorr, respectively. The $PbTiO_3$ and the $SrTiO_3$ layers of the superlattices were grown at same conditions at 600°C growth temperature and 100 mTorr oxygen pressure. The fluence of laser pulses was 1.5 J/cm^2 with a repetition rate of 10 Hz. Reflection high-energy electron diffraction (RHEED) was used during the deposition to ensure the maintenance of layer-by-layer growth mode of $PbTiO_3$ and $SrTiO_3$ throughout the growth process. This enables the total thickness of the superlattices to be kept at100 nm, while the periodicity of the superlattices differs. After depositions, the superlattices were annealed for 10 min in 50 Torr oxygen pressure to promote full oxidation and then cooled down to room temperature at that oxygen pressure.

STEM Analysis. The plane-view samples of the superlattices for the STEM experiments were prepared by gluing a 2.5 mm × 2.5 mm film on a 3-mm molybdenum grid. The plane-view samples were then grinded, dimpled and ion-milled. Cross-sectional samples for the dark-field TEM and STEM experiments were prepared by slicing, gluing, grinding, dimpling and ion milling. A Gatan PIPS II was used for the final ion milling. Before ion milling, the samples were dimpled down to less than 20 μm. The final ion-milling voltage was 0.5 kV to reduce ion-beam damage. HAADF-STEM images were recorded by using a Cs-corrected TEAM1 FEI Titan microscope working at 300 kV. A HAADF detector acquiring 'Z-contrast' images were used to record the HAADF-STEM images.

The beam convergence angle was 17 mrad. The diffraction contrast image (Fig. 1b) was recorded using a TitanX microscope (FEI) working at 300 kV. Determination and mapping of the polar atomic displacements was performed on the atomic-scale HAADF-STEM images by using the column offsets of each titanium and lead atom, obtained from the position fitting of the titanium and lead atoms. The atom positions were determined by fitting them as two-dimensional Gaussian peaks using Matlab. The titanium displacement in each $PbTiO_3$ unit cell was calculated as a vector between each titanium atom and the center of mass of its four nearest lead neighbors. The displacement of the titanium in each unit cell was opposite to the polarization direction of the $PbTiO_3$. The visualization of the two-dimensional polar displacement vectors was carried out using Matlab. Random noise in the displacement vector maps was reduced using a weighted smoothing length of 1.2 nm.

In-situ STEM study. In situ characterization was performed using dark-field (DF) diffraction contrast TEM on a JEOL 3010 at 300kV. This method provides rapid acquisition (30ms frame time) and sensitivity to the polarization direction from dynamic scattering arising from the non-centro-symmetry of the crystal along the selected Bragg peak. An electrical bias was applied using an external power supply along the cross-section of the sample via a freely positioned tungsten probe at the superlattice surface biased to the conductive SRO bottom bottom electrode (Fig. 3).

Phase-field Simulation. Quasi 2-Dimensional Phase-field simulations are performed to study polarization distribution in $(PbTiO_3)_6/(SrTiO_3)_6$ superlattice on a $(110)_o$-$DyScO_3$ substrate. The spontaneous polarization vector P is used as the order parameter. The temporal evolution of the order parameter is governed by time dependent Ginsburg-Landau equation, i.e.,

$$\frac{\partial P_i}{\partial t} = -L \frac{\delta F}{\delta P_i} \left(i = 1,3 \right)$$

Where t is the evolution time, L is the kinetic coefficient related to the mobility of the domain wall. The total free energy F has the contributions from mechanical, electrostatic, Landau chemical and polarization gradient energies,

$$F = \int \left(f_{Elastic} + f_{Electric} + f_{Landau} + f_{Gradient} \right) dV$$

Detailed expressions of the energy terms, the material parameters as well as how to numerically solve the equations have been given in previous literatures.[23, 31-33] The simulation system is discretized into a quasi-2D grid of $400\Delta x \times 4\Delta y \times 250\Delta z$, with $\Delta x = \Delta y = \Delta z = 0.4$ nm. Periodic boundary condition is applied along the inplane dimensions, while a superposition method is used in the out-of-plane direction.[34] In the out-of-plane dimension, the thickness of the substrate, film and air are set as $30\Delta z$, $188\Delta z$ and $32\Delta z$, respectively; while the film is comprised of periodical stacking of $6\Delta z$ of $PbTiO_3$ layers and $6\Delta z$ of $SrTiO_3$ layers. Close-circuit electric boundary condition is used where the electric potential is fixed to zero at the top and bottom of the film surface.[31] While a thin film boundary condition is applied where the stress on the top of the thin film is zero, and at the bottom of the substrate far away from the film/substrate interface, the displacement is zero.[32] Iteration perturbation method is used to account for the inhomogeneity in the elastic constants of $PbTiO_3$ and $SrTiO_3$.[35] The lattice constant of the substrate is set as 3.947 Å (fully strained along X) and 3.942 Å (partial relaxation in a thin TEM sample along Y). A background dielectric constant of 40 is used.[36, 37] A tail-to-tail charged domain wall is set as the initial configuration. The time step interval is set as 0.01, the simulation runs for a total of 40000 timesteps. To simulate the applied electric field through the Tungsten tip, a Lorentz-type electric potential function is applied on the top of the thin film, i.e., $\varphi=\varphi_0\frac{\gamma^2}{\gamma^2+(x-x_0)^2+(y-y_0)^2}$, where $\varphi_0$is the magnitude of the applied electric potential, the tip effective radius $\gamma$is set as 20 nm, the tip position (x_0, y_0) is set on the middle of the film top, i.e., (200 Δx, 2 Δy).

Acknowledgements

R.R. acknowledges support from the Office of Basic Energy Sciences, US Department of Energy (DE-AC02-05CH11231). The work is supported by the Computational Materials Sciences Program funded by the US Department of Energy, Office of Science, Basic Energy Sciences, under Award Number DE-SC0020145 (L.Q.C.). L.Q.C. and L.W.M. acknowledges support from the U.S. Department of Energy, Office of Science, Office of Basic Energy Sciences, under Award Number DE-SC-0012375 for the development of novel ferroic heterostructures. Z.H. acknowledges the Extreme Science and Engineering Discovery Environment (XSEDE) cluster, which is supported by National Science Foundation grant number ACI-1548562, and specifically, it used the Bridges system, which is supported by NSF award number ACI-1445606, at the Pittsburgh Supercomputing Center (PSC),[38, 39] under the allocation DMR170006. Electron microscopy of superlattice structures was performed at the Molecular Foundry, LBNL, supported by the Office of Science, Office of Basic Energy Sciences, US Department of Energy (DE-AC02-05CH11231).

Author Contributions

S.D. and R.R. designed the experiments. S.D., A.Y carried out the synthesis and characterization of superlattice samples. C.N. performed TEM characterization including bias experiments of the samples, along with the detailed polarization vector analysis. Z.H. performed and analyzed phase-field calculations for these samples. S.D. Z.H. and R.R. analyzed the data and co-wrote the manuscript. L.C., Y. W., L.W. M. and R.R. supervised the research. All authors contributed to the discussion and manuscript preparation.

Competing financial interests

The authors declare no competing financial interests.

References

[1] V. Estévez, L. Laurson, Head-to-head domain wall structures in wide permalloy strips. *Phys. Rev. B* **91**, 054407 (2015).

[2] S. S. P. Parkin, M. Hayashi, L. Thomas, Magnetic Domain Wall Racetrack Memory. *Science* **320**, 190-194 (2008).

[3] K. A. Omari, T. J. Hayward, Chirality Based Vortex Domain-Wall Logic Gates. *Phys. Rev. Appl.* **2**, 044001 (2014).

[4] D. A. Allwood *et al.*, Magnetic Domain Wall Logic. *Science* **309**, 1688-1692 (2005).

[5] A. M. Glazer, S. A. Mabud, Powder profile refinement of lead zirconate titanate at several temperatures. II. Pure $PbTiO_3$. *Acta Crystallographica Section B-Structural Science* **34**, 1065-1070 (1978).

[6] B. Meyer and D. Vanderbilt, *Phys. Rev. B* **65**, 104111 (2002).

[7] S. Cherifi-Hertel *et al.*, Non-Ising and chiral ferroelectric domain walls revealed by nonlinear optical microscopy. *Nat. Commun.* **8**, 15768 (2017).

[8] E. A. Eliseev *et al.*, Surface effect on domain wall width in ferroelectrics. *Journal of Applied Physics* **106**, 084102 (2009).

[9] C.-L. Jia *et al.*, Direct Observation of Continuous Electric Dipole Rotation in Flux-Closure Domains in Ferroelectric $Pb(Zr,Ti)O_3$. *Science* **331**, 1420-1423 (2011).

[10] C. T. Nelson *et al.*, Spontaneous vortex nanodomain arrays at ferroelectric heterointerfaces. *Nano Lett.* **11**, 828-834 (2011).

[11] Y. L. Tang *et al.*, Observation of a periodic array of flux-closure quadrants in strained ferroelectric $PbTiO_3$ films. *Science* **348**, 547-551 (2015).

[12] V. Estévez, L. Laurson, Head-to-head domain wall structures in wide permalloy strips. *Phys. Rev. B* **91**, 054407 (2015).

[13] D. Meier *et al.*, Anisotropic conductance at improper ferroelectric domain walls. *Nat. Mater.* **11**, 284-288 (2012).

[14] M. Y. Gureev, A. K. Tagantsev, N. Setter, in *2009 18th IEEE International Symposium on the Applications of Ferroelectrics*. (2009), pp. 1-6.

[15] X. Wu, D. Vanderbilt, Theory of hypothetical ferroelectric superlattices incorporating head-to-head and tail-to-tail 180 domain walls. *Phys. Rev. B* **73**, 020103 (2006).

[16] P. S. Bednyakov, T. Sluka, A. K. Tagantsev, D. Damjanovic, N. Setter, Formation of charged ferroelectric domain walls with controlled periodicity. *Sci. Rep.* **5**, 15819 (2015).

[17] T. Kämpfe *et al.*, Optical three-dimensional profiling of charged domain walls in ferroelectrics by Cherenkov second-harmonic generation. *Phys. Rev. B* **89**, 035314 (2014).

[18] L. Li *et al.*, Giant Resistive Switching via Control of Ferroelectric Charged Domain Walls. *Adv. Mater.* **28**, 6574-6580 (2016).

[19] N. Balke *et al.*, Direct Observation of Capacitor Switching Using Planar Electrodes. *Adv. Func. Mater.* **20**, 3466-3475 (2010).

[20] P. Gao *et al.*, Direct Observations of Retention Failure in Ferroelectric Memories. *Adv. Mater.* **24**, 1106-1110 (2012).

[21] W.-M. Lee *et al.*, Spatially Resolved Photodetection in Leaky Ferroelectric BiFeO3. *Adv. Mater.* **24**, OP49-OP53 (2012).

[22] A. K. Yadav *et al.*, Observation of polar vortices in oxide superlattices. *Nature* **530**, 198 (2016).

[23] Z. Hong, et al. Stability of polar vortex lattice in ferroelectric superlattices. *Nano Lett.* **17**, 2246–2252 (2017).

[24] S. Hsu, et al. Emergence of the Vortex State in Confined Ferroelectric Heterostructures. *Adv. Mater.* **31 (36)**, 1901014 (2019).

[25] N. Balke *et al.*, Enhanced electric conductivity at ferroelectric vortex cores in $BiFeO_3$. *Nat. Phys.* **8**, 81 (2011).

[26] A. R. Damodaran *et al.*, Phase coexistence and electric-field control of toroidal order in oxide superlattices. *Nat. Mater.* **16**, 1003 (2017).

[27] A. K. Yadav *et al.*, Spatially resolved steady-state negative capacitance, *Nature* **565**, 468–471 (2019).

[28] P. Shafer *et al.*, Emergent chirality in the electric polarization texture of titanate superlattices. *Proc. Natl. Acad. Sci. U.S.A*, **115 (5)** 915-920 (2018).

[29] Z. Hong *et al.*, Local 90° switching in $Pb(Zr_{0.2}Ti_{0.8})O_3$ thin film: Phase-field modeling. *Acta Mater.* **73**, 75 (2014).

[30] S. Prosandeev, I. Ponomareva, I. Kornev, and L. Bellaiche. Control of Vortices by Homogeneous Fields in Asymmetric Ferroelectric and Ferromagnetic Rings. *Phys. Rev. Lett.* **100**, 047201 (2008)

[31] L. Chen, Phase-field model of phase transitions/domain structures in ferroelectric thin films: a review. *J. Am. Ceram. Soc.* **91**, 1835–1844 (2008).

[32] Y. Li, S. Hu, Z. Liu & L. Chen, Effect of electrical boundary conditions on ferroelectric domain structures in thin films. *Appl. Phys. Lett.* **81**, 427–429 (2002).

[33] Y. Li, S. Hu, Z. Liu & L. Chen, Effect of substrate constraint on the stability and evolution of ferroelectric domain structures in thin films. *Acta Mater.* **50**, 395–411 (2002).

[34] L. Chen, J. Shen, Applications of semi-implicit Fourier-spectral method to phase field equations. *Comput. Phys. Commun.* 108(2–3), 147 (1998).

[35] J. Wang, X. Ma, Q. Li, J. Britson & L. Chen, Phase transitions and domain structures of ferroelectric nanoparticles: phase field model incorporating strong elastic and dielectric inhomogeneity. *Acta Mater.* **61**, 7591–7603 (2013).

[36] A. Tagantsev, The role of background dielectric susceptibility in uniaxial ferroelectrics. *Ferroelectrics* **69**, 321–323 (1986).

[37] Y. Zheng & C. Woo, Giant piezoelectric resistance in ferroelectric tunnel junctions. *Nanotechnology* **20**, 075401 (2009).

[38] J. Towns, T. Cockerill, M. Dahan, I. Foster, K. Gaither, A. Grimshaw, V. Hazlewood, S. Lathrop, D. Lifka, G.D. Peterson, R. Roskies, J.R. Scott, and N. Wilkens-Diehr, XSEDE: Accelerating Scientific Discovery. *Comput. Sci. Eng.* **16(5)**, 62- 74 (2014).

[39] N. A. Nystrom, M. J. Levine, R. Z. Roskies, and J. R. Scott, Bridges: A Uniquely Flexible HPC Resource for New Communities and Data Analytics. In Proceedings of the 2015 Annual Conference on Extreme Science and Engineering Discovery Environment (St. Louis, MO, July 26-30, 2015). XSEDE15. ACM, New York, NY, USA.

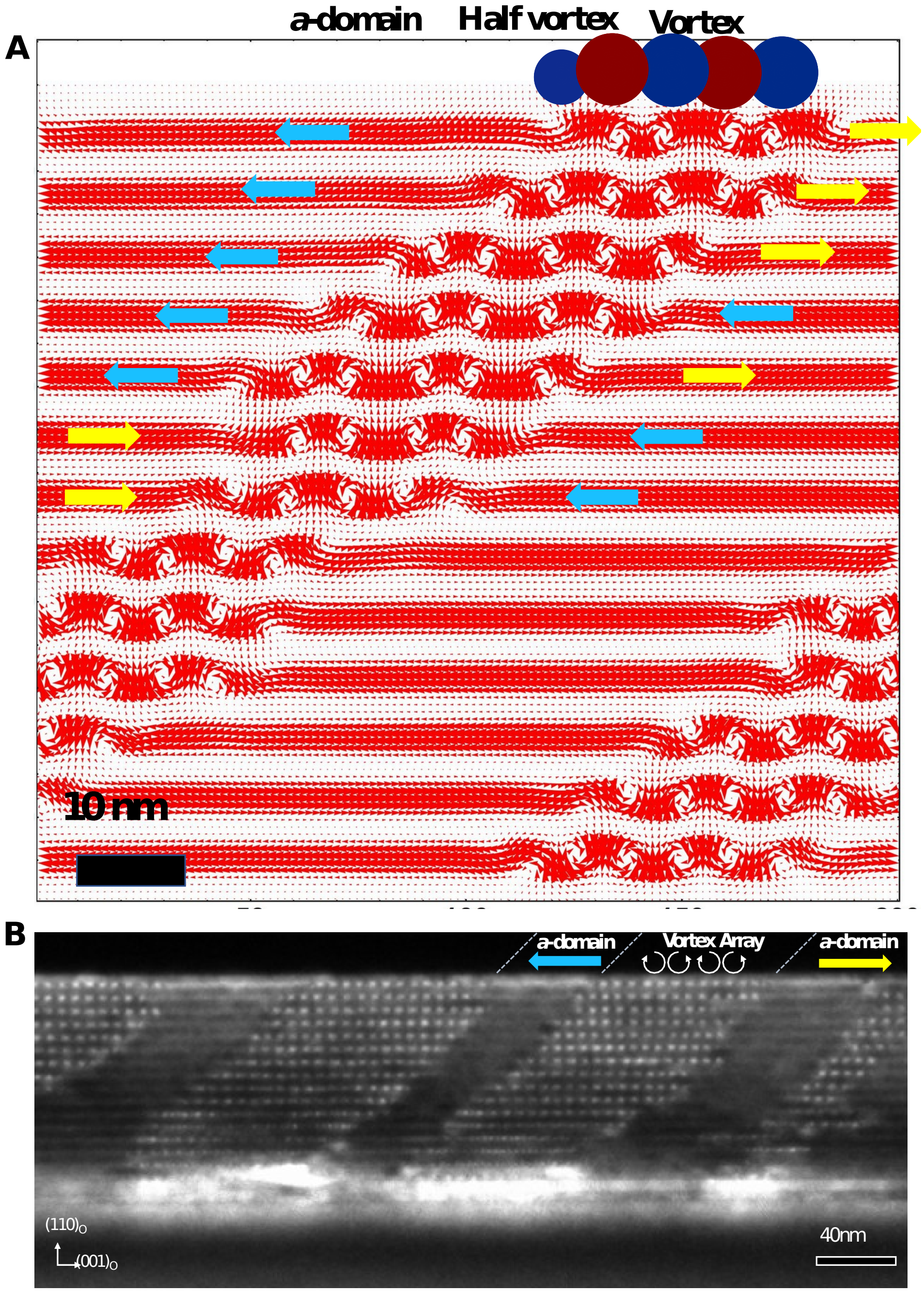

Fig. 1| Structure of mixed states vortices and *a* domains. A, Low magnification, STEM image of the cross-section of a $(PbTiO_3)_8/(SrTiO_3)_8$ superlattice along the $[010]_{pc}$ zone axis. Each bright/dark modulation corresponds to a period of the clockwise vortex–counter clockwise vortex strings. The phase separates into roughly periodic blocks of vortices (vortex strings) and *a*-domains such a way that domain walls form on $\{101\}_{pc}$. The presence of vortex strings is being laterally bounded by antiparallel *a* domains (head to head or tail to tail) which would nominally form a CDW if vortex string were absent. **B,** Phase-field simulations shows the MVDs string stabilized CDW (tail-to-tail domain walls as well as head-to-head) and neutral domain walls. The formation of domain walls on $\{101\}_{pc}$ are also captured.

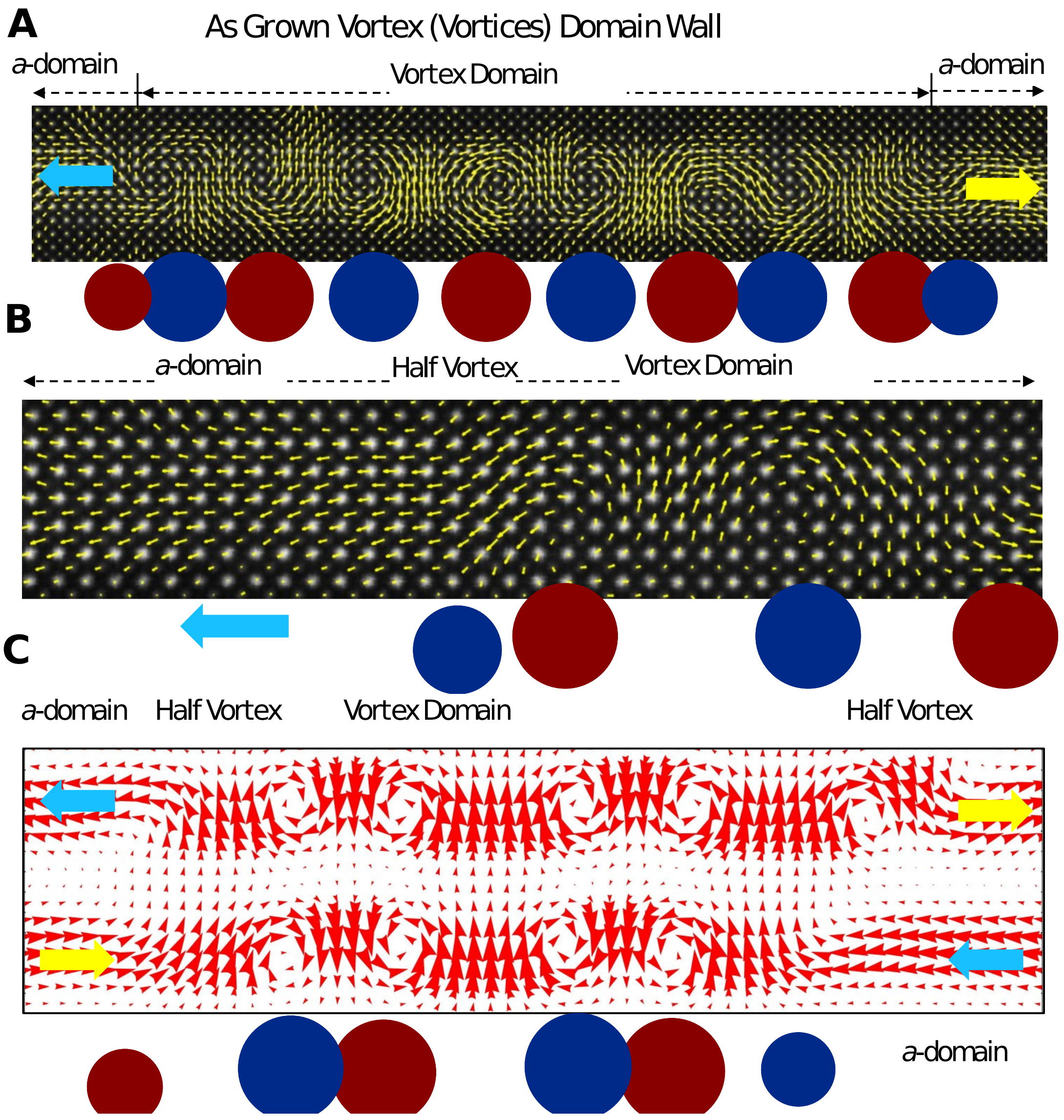

Fig. 2| High-resolution presentation of the vortex-domain wall. **A,** High resolution-STEM image with an overlay of the polar displacement vectors ($\boldsymbol{P}_{\mathrm{D}}$, indicated by arrows) with alternate clockwise and anticlockwise vortices of polarization and with *a* domains (middle panel). Yellow arrow indicates positive $\boldsymbol{P}_{\mathrm{x}}$ and blue arrow shows negative $\boldsymbol{P}_{\mathrm{x}}$. **B,** High resolution image of the boundary on the left side of A. **C,** High resolution image of the phase-field result, showing both the head-to-head and tail-to-tail domain wall.

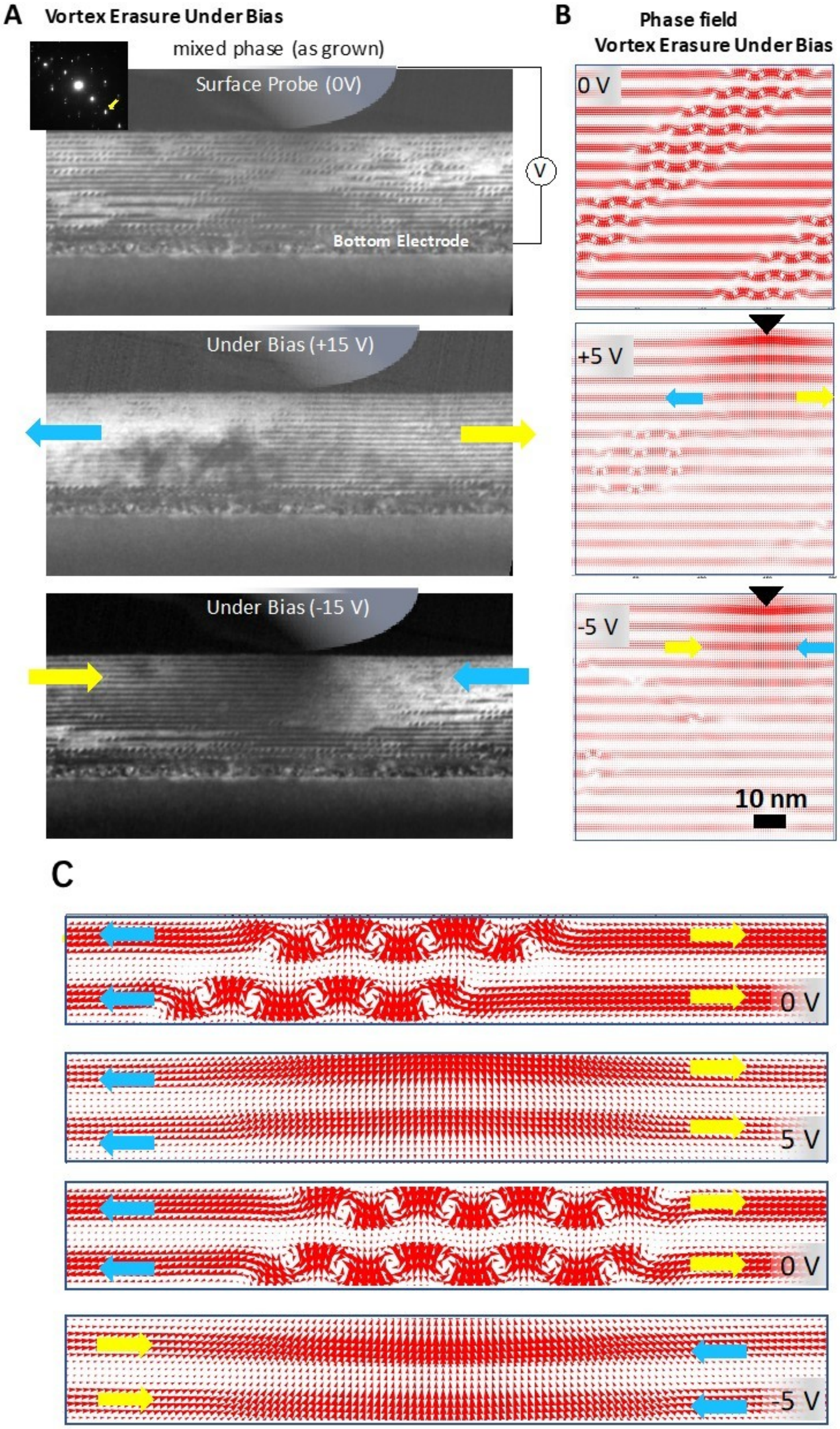

Fig. 3| Creation of MVDWs and CDWs under *in situ* electric field in $(PbTiO_3)_6/(SrTiO_3)_6$ superlattice.

A, Applying the biased through the tungsten probe to the grounded bottom electrode in the cross-section of the $(PbTiO_3)_6/(SrTiO_3)_6$ superlattice which has mixed phase state of vortices and a-domains observed by DF-TEM image. Under applied the positive bias (+15V) the vortex strings erase and form the tail-to-tail domain walls (middle pattern) and under the negative bias (-15V) some of vortex strings reappear and form the head-to-head domain walls (bottom panel). **B**, Phase field simulation of the electric field control of CDWs creations. As grown condition superlattice shows mixed states of vortex and a-domains (top panel). After applying the +5V the vortex phase erase and create tail-to-tail domain walls (middle panel) and after applied -5V vortex reappear including head-to-head domain walls (bottom panel). **C**, Concept of vortex domain wall memory as simulated by phase-field. Applying external electric field through a tip electrode could trigger the transition between multi-VDWs and CDWs.

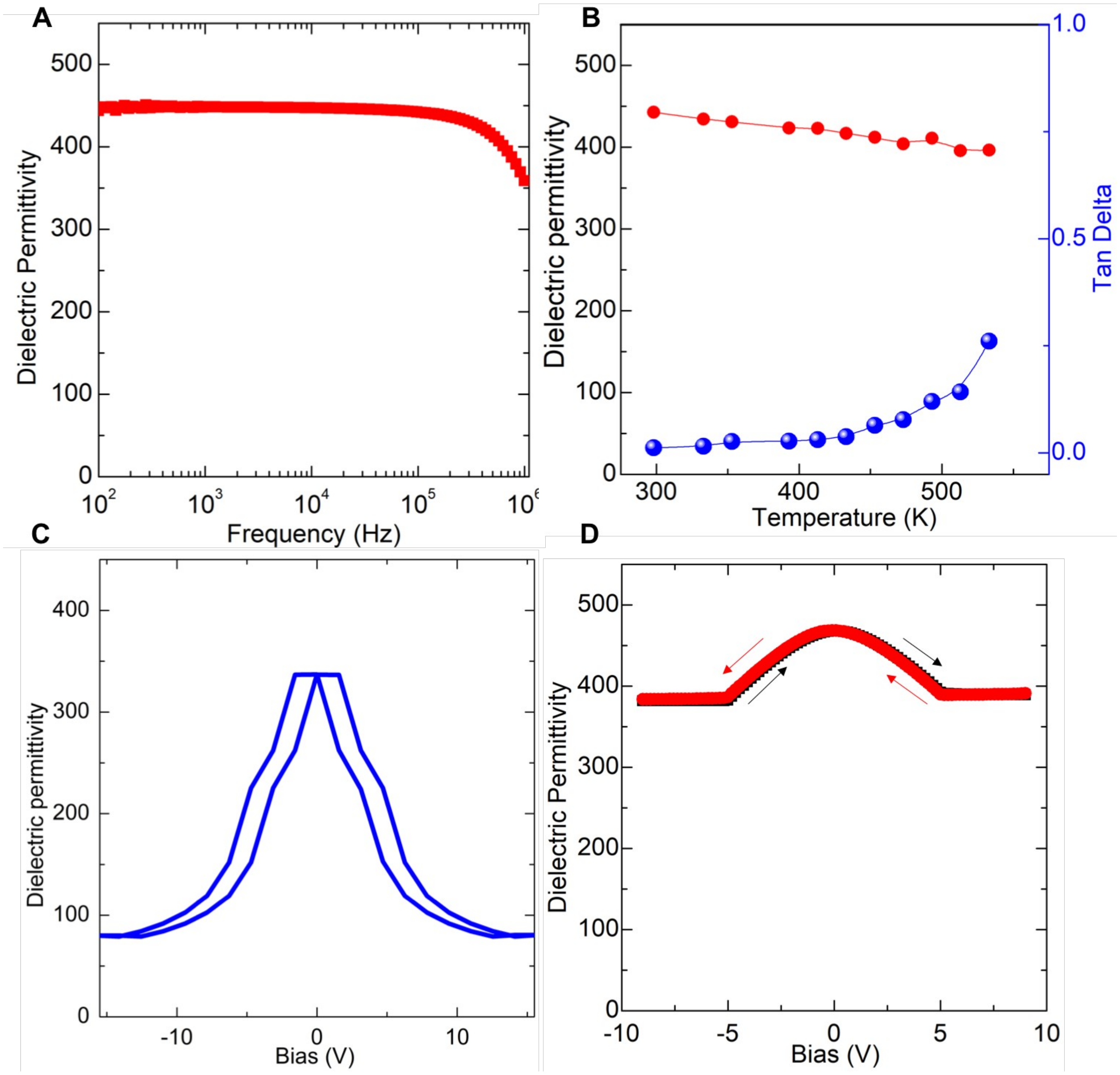

Fig. 4| Dielectric properties of the $(PbTiO_3)_6/(SrTiO_3)_6$ superlattice. A, Frequency dependent of the dielectric permittivity under zero voltage, showing very stable dielectric permittivity over a large range of frequencies. **B,** Permittivity as a function of temperature at 10 kHz. The permittivity is also very stable over a temperature range of >150 K. **C,** Permittivity vs. bias loop as calculated by phase-field simulations. **D,** corresponding experimental measurements.

Supplementary

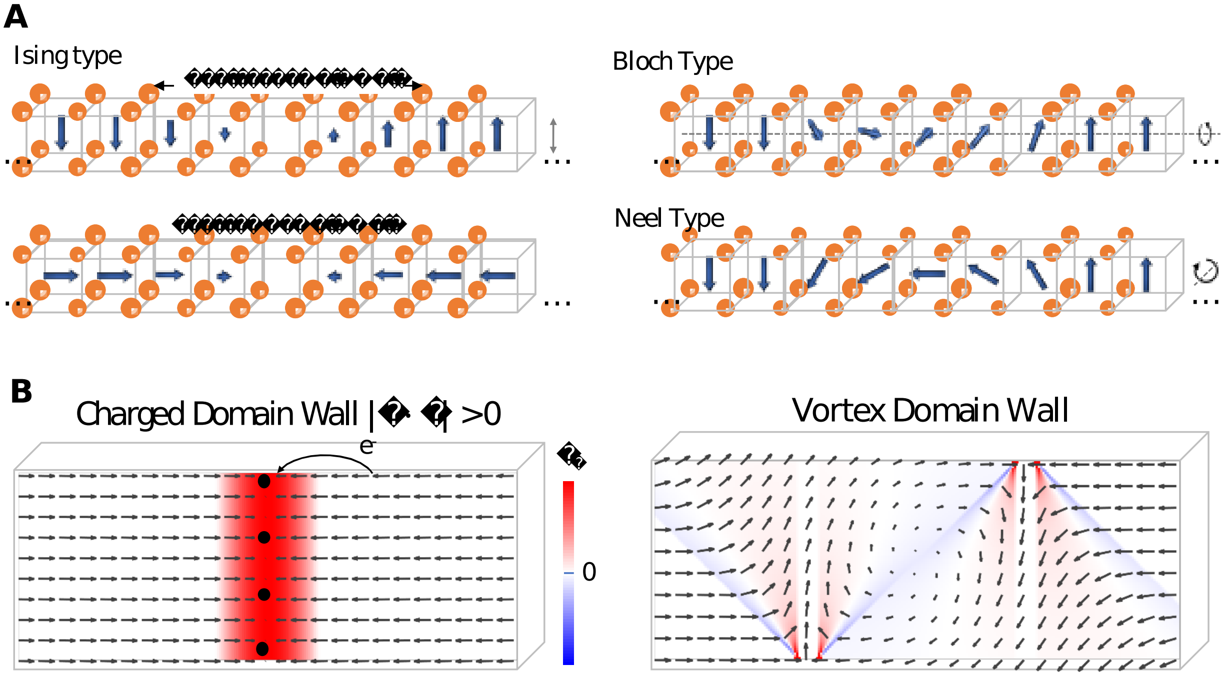

Fig. S1| Domain wall structures. A, Schematic representation of Ising walls (neutral and charged), Nèel and Bloch type domain walls. The Nèel and Bloch walls are classified by their axis of rigid rotation. **B,** Schematic view of 180° head-to-head charged domain walls normal to the polarization axis (top left), anisotropic transverse domain walls (bottom left), isotopic transverse domain walls (top right) and vortex domain walls (VDWs) (bottom right).

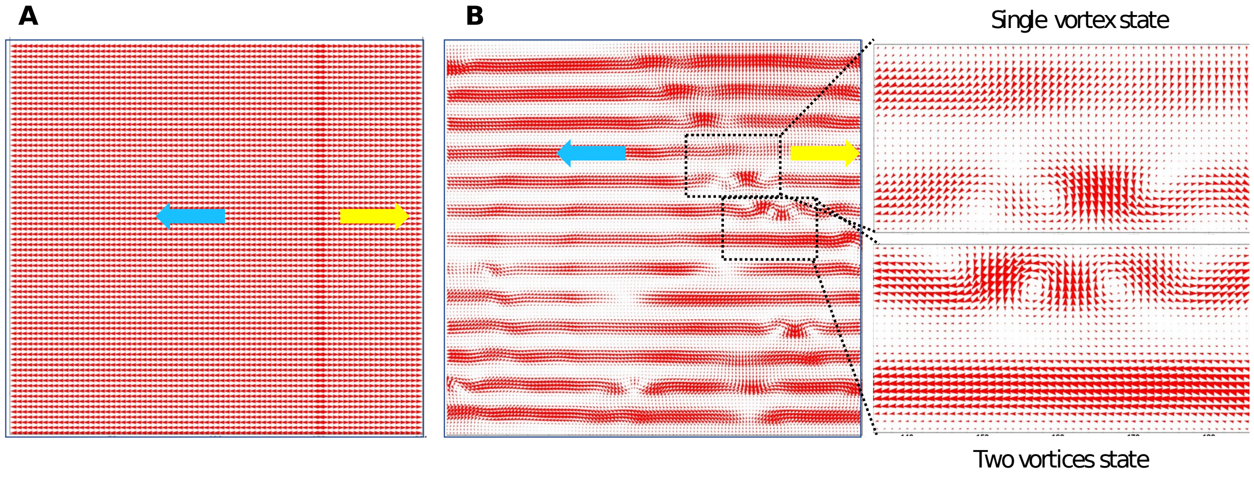

Fig. S2| The dynamic formation of the vortex domain wall for $(PTO)_6/(STO)_6$. A, Initial setup **B,** intermediate metastable state with only one or two vortices in between the charged *a*-domain wall.

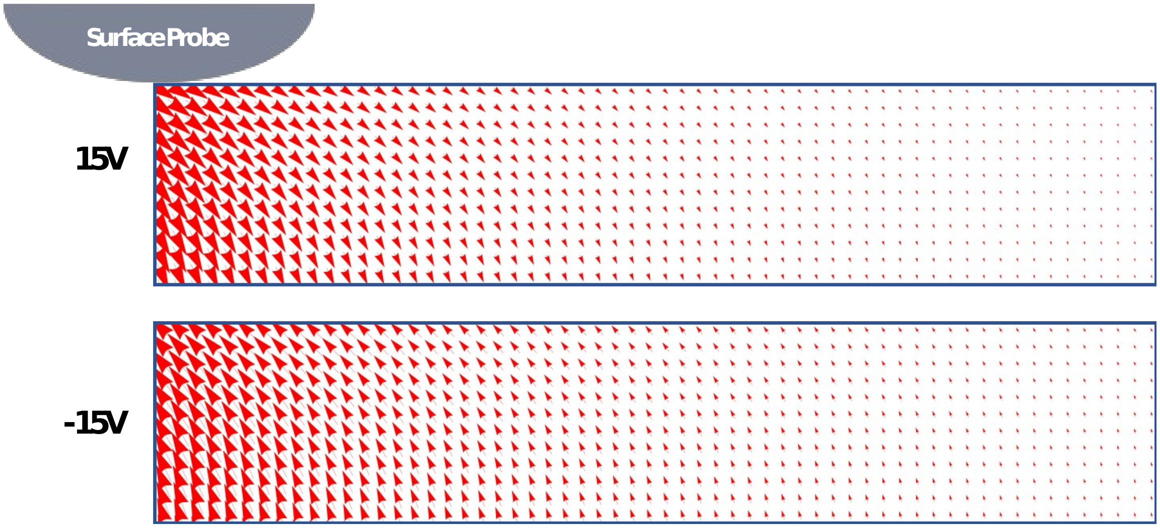

Fig. S3| Direction of the applied electric field underneath the tip with different applied electric potential through a surface probe calculated by phase-field.